Supplementary Information for

Crucial role of subsurface ocean variability in tropical cyclone genesis

Cong Gao, Lei Zhou*, I.-I. Lin, Chunzai Wang, Shoude Guan, Fei-Fei Jin, Raghu Murtugudde

*Corresponding author. e-mail: zhoulei1588@sjtu.edu.cn

This file includes:

Supplementary Fig. 1 to Supplementary Fig. 10

Supplementary Table 1 to Supplementary Table 3

Supplementary References

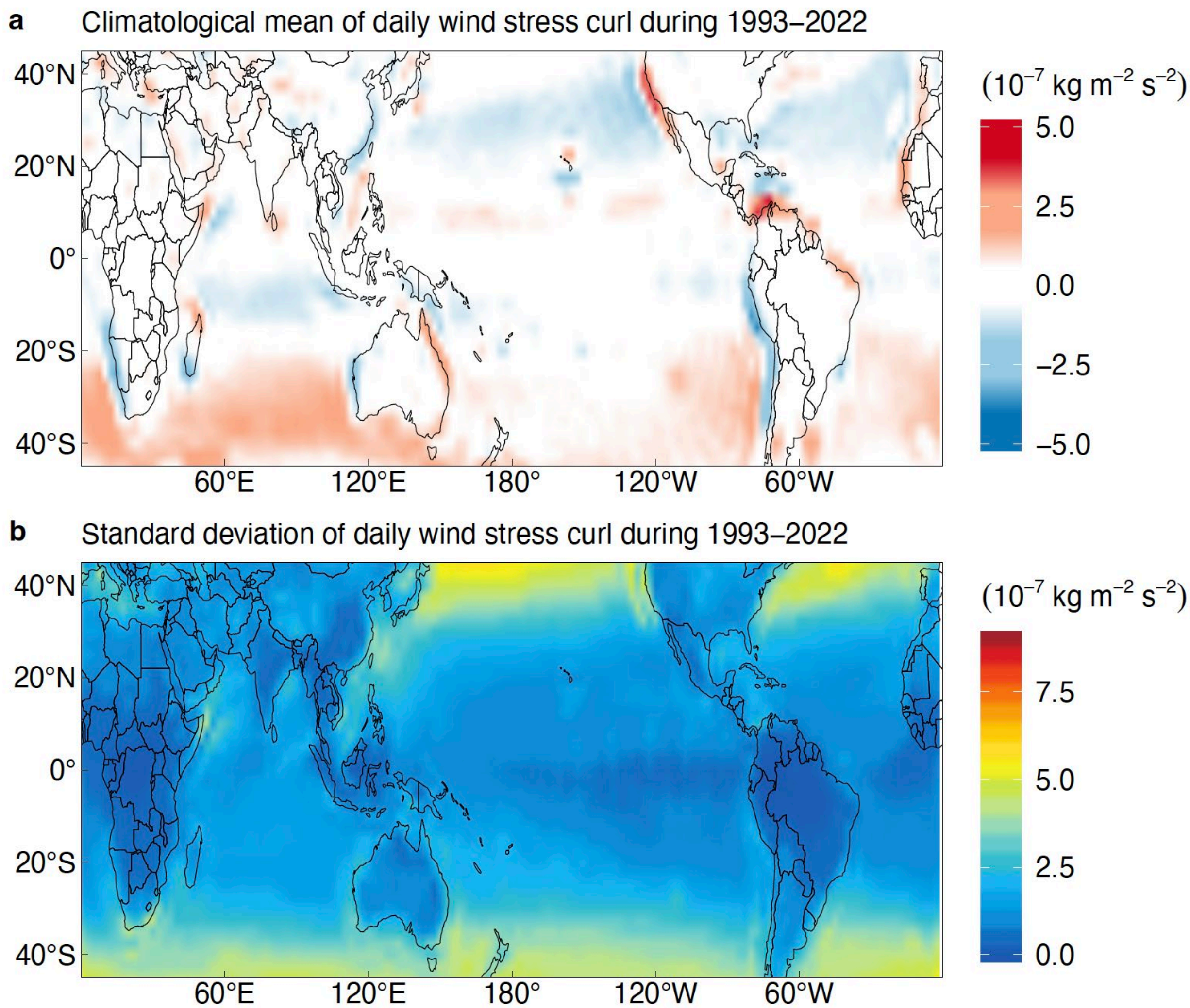

Supplementary Fig. 1 | Global distribution of near-surface wind stress curl. **a**, Thirty-year mean daily wind stress curl at sigma level 995 in atmosphere. **b**, Standard deviation of daily wind stress curl at sigma level 995 in atmosphere.

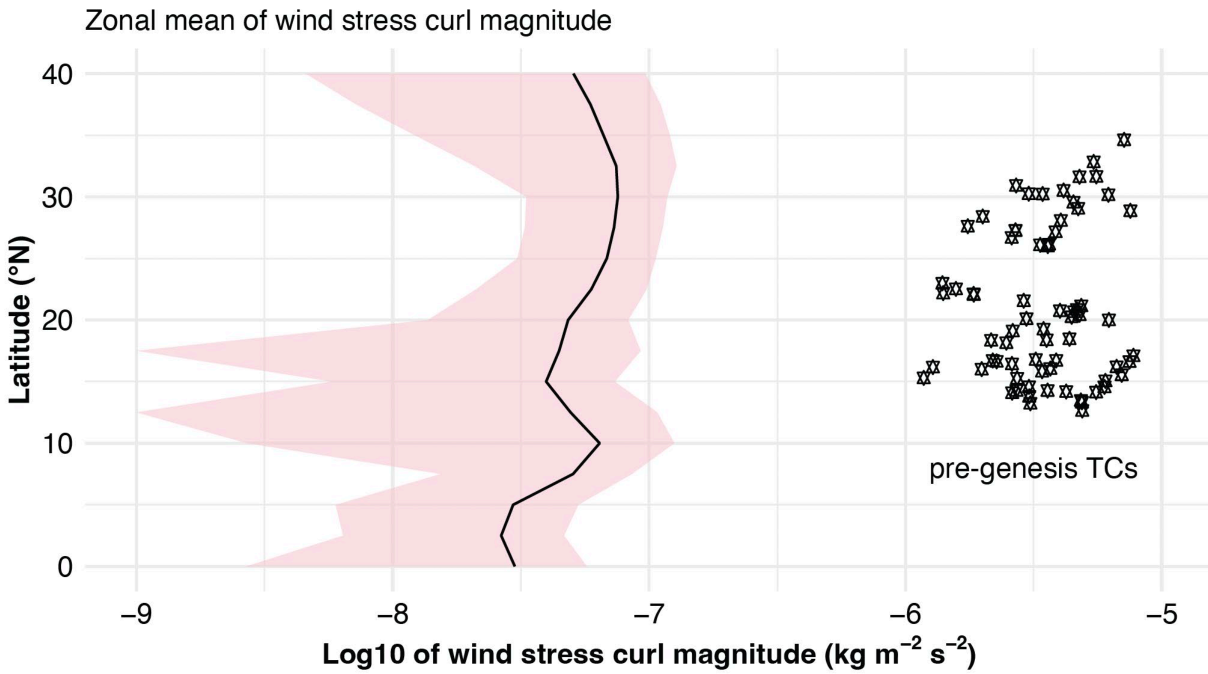

Supplementary Fig. 2 | Comparisons of near-surface wind stress curl between the climatologies and the pre-genesis TCs. Black line shows the zonal mean wind stress curl at sigma level 995. Shading represents the standard deviation of the near-surface wind stress curl. Hexagons denote the mean wind stress curl in a circle with a 100 km radius centred around the pre-genesis TCs. Note that the intensities of pre-genesis TCs range from 15 to 18 m s^{-1}.

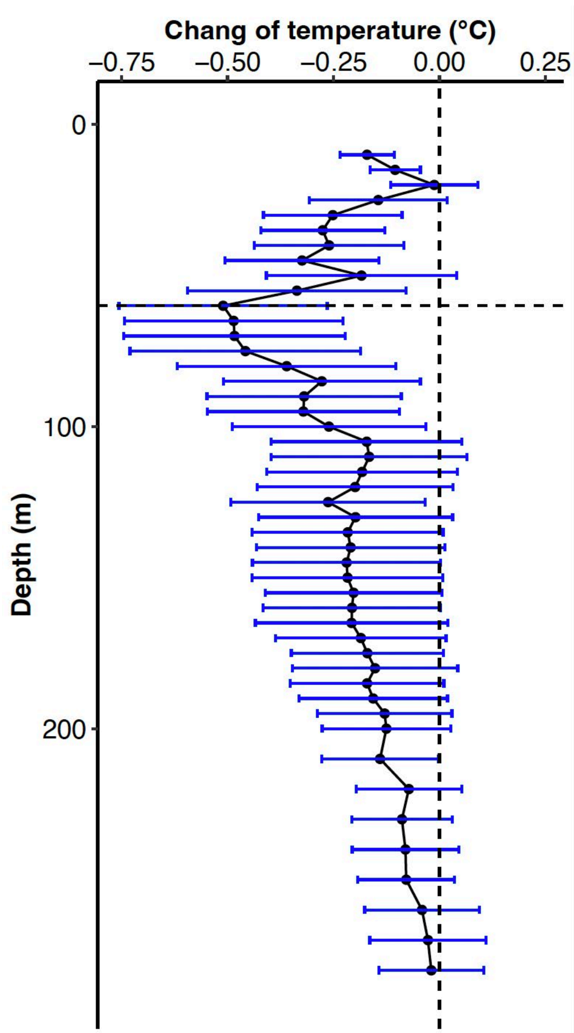

Supplementary Fig. 3 | Composite changes in ocean temperature profiles due to pre-genesis TCs based on the Argo float data. The black points denote the mean ocean temperature changes. The blue error bars denote the corresponding standard errors of the mean (SEM). Horizontal dotted line denotes the composite mean D26 (60 m).

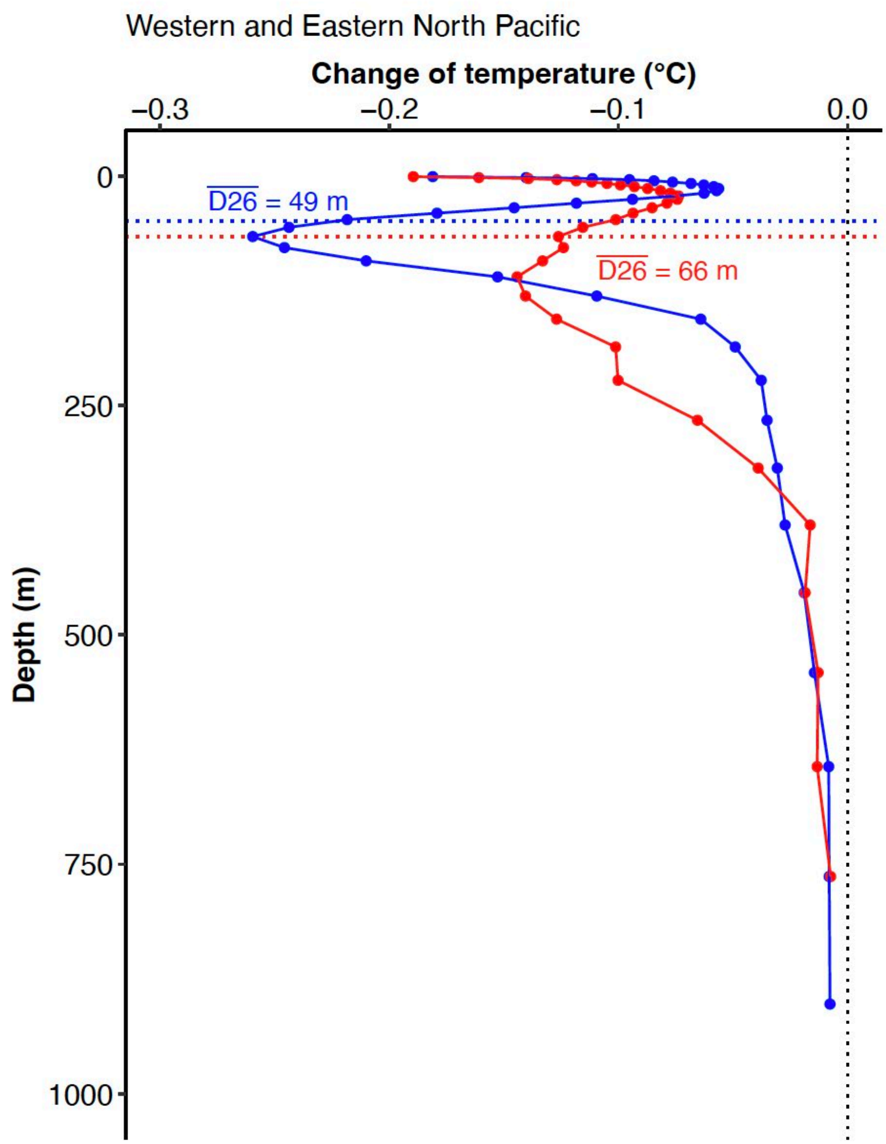

Supplementary Fig. 4 | Composite changes in ocean temperature profiles due to pre-genesis TCs in the western and the eastern North Pacific. Red (blue) dots and lines are for the western (eastern) North Pacific with the composited mean D26 of 66 (49) m. The western North Pacific is within 0°–40°N and 100°E–180°; the eastern Pacific is within 0°–40°N and 180°–100°W.

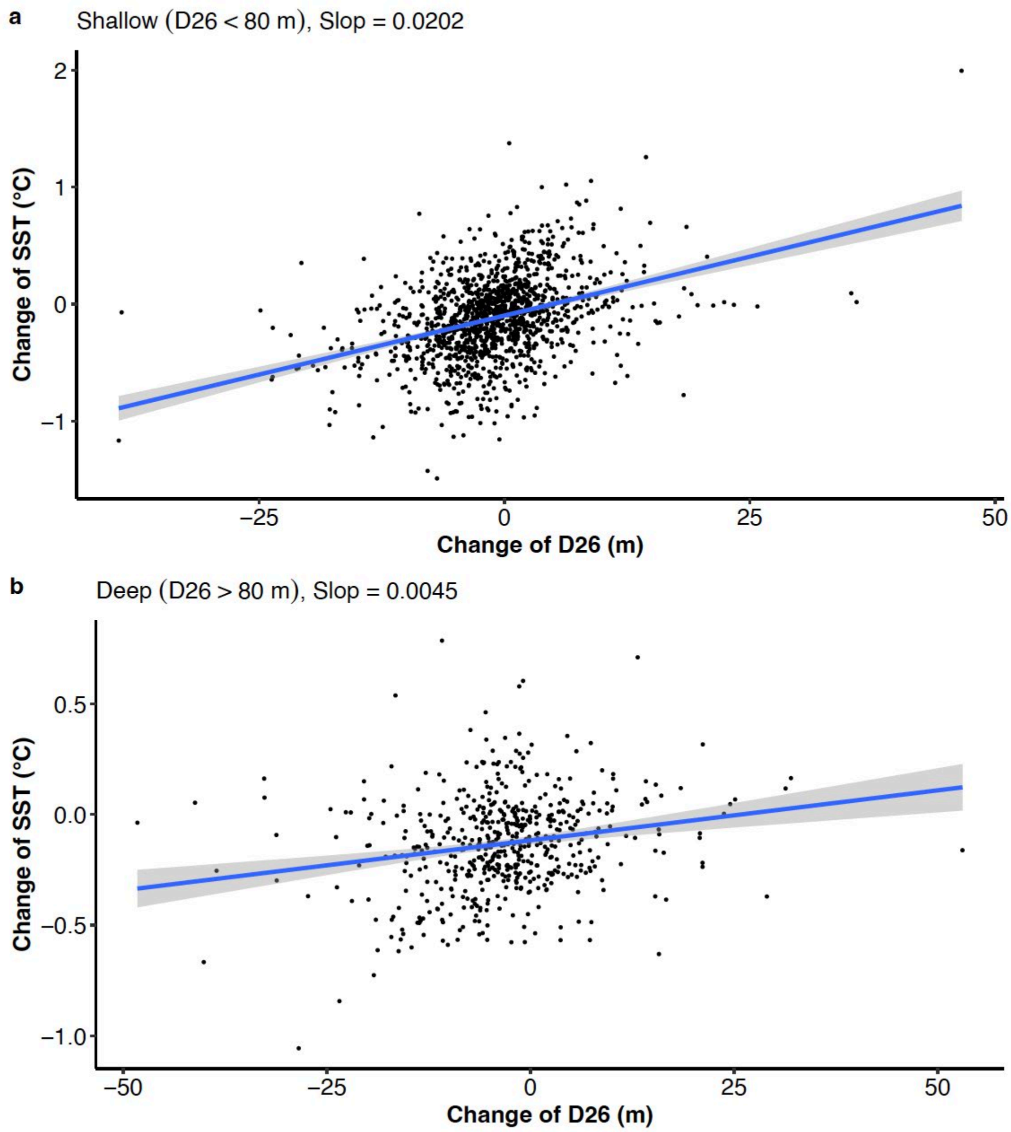

Supplementary Fig. 5 | Influences of background D26 on the relationship between SST anomalies and D26 anomalies during pre-genesis TCs. a, Same as Fig. 5a but for the shallow background D26 (< 80 m). **b**, Same as Fig. 5a but for the deep background D26 (> 80 m).

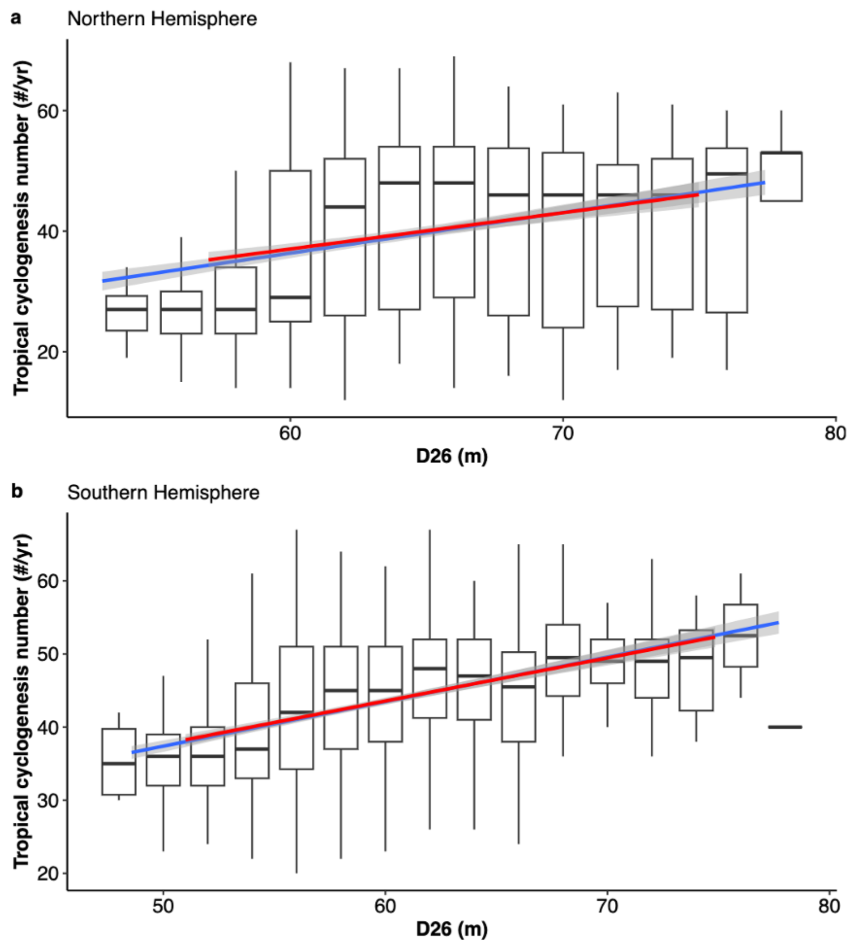

Supplementary Fig. 6 | Dependence of tropical cyclogenesis on D26 in HighResMIP models. **a**, Boxplots of tropical cyclogenesis numbers for different D26 in the Northern Hemisphere. The central line of the box represents the median of the data. The upper and lower edges of the box indicate the first (Q1) and third quartiles (Q3), representing the interquartile range (IQR). The abscissa denotes the annual mean D26 from July to September over the tropics (0°–20°N) in the Northern Hemisphere. The ordinate denotes the total tropical cyclogenesis numbers from July to September over the tropics in the Northern Hemisphere. **b**, Same as **a** but from January to March over the tropics (20°S–0°) in the Southern Hemisphere. Blue lines with grey shading denote simple linear regressions with 95% confidence intervals. Red lines are the same as the blue lines but with the removal of the first two groups and the last two groups.

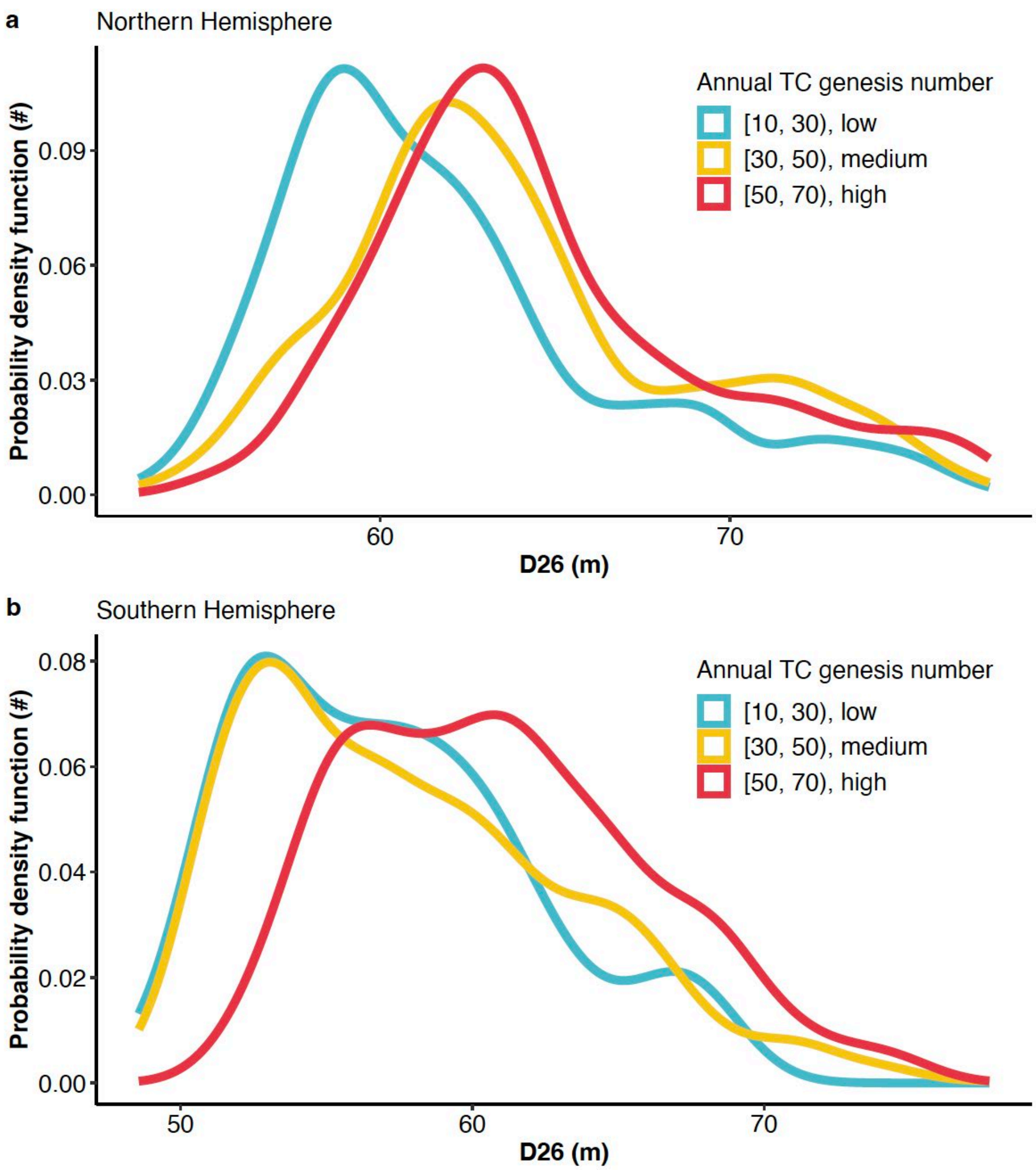

Supplementary Fig. 7 | Probability density functions of D26 under various TC genesis conditions in HighResMIP models. **a**, The annual mean D26 from July to September over the tropics (0°–20°N) in the Northern Hemisphere is divided into three groups based on annual TC genesis number. The D26 probability functions of low (10–30), medium (30–50) and high (50–70) TC genesis number group are shown by blue, yellow and red, respectively. **b**, Same as **a** but from January to March over the tropics (20°S–0°) in the Southern Hemisphere.

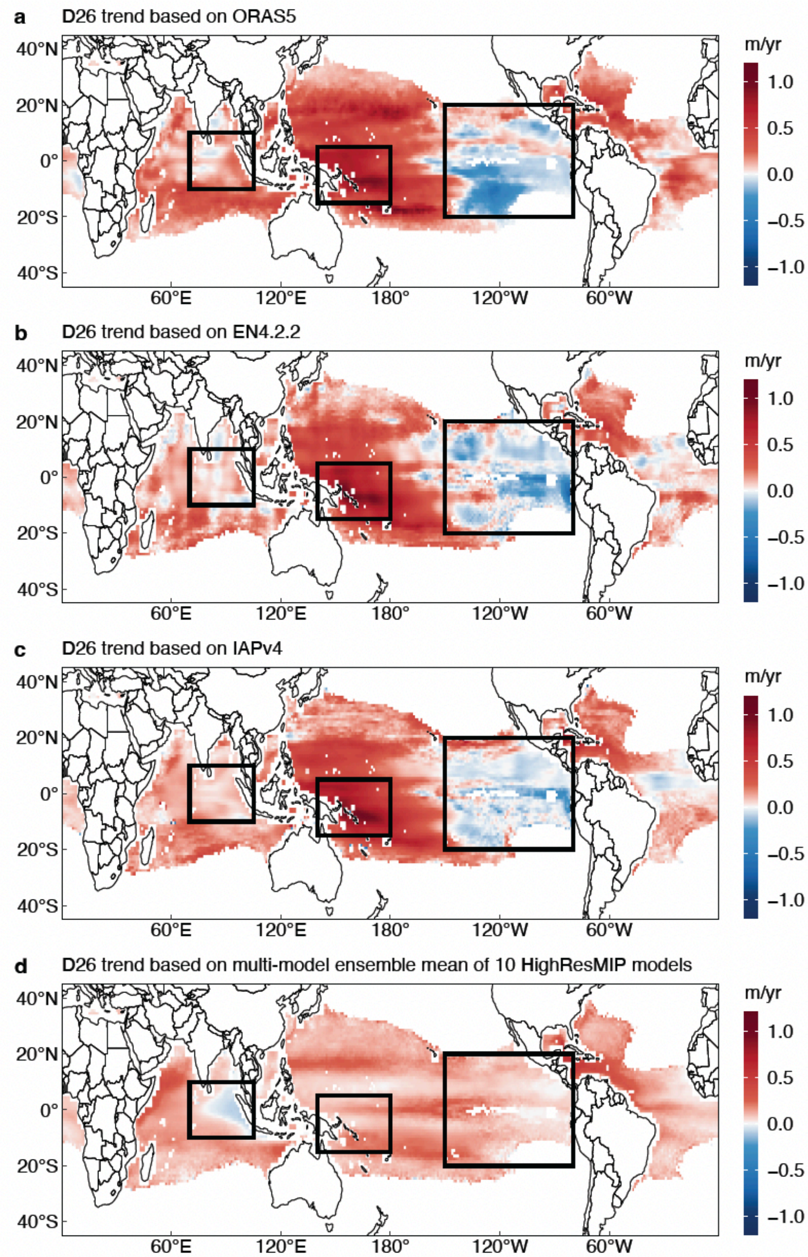

Supplementary Fig. 8 | Comparisons of D26 trends between the observations and the simulations by 10 HighResMIP models. **a**, D26 trends from 1980 to 2022 derived from the ORAS5 reanalysis. **b**, Same as **a** but derived from EN4.2.2 analysis. **c**, Same as **a** but derived from IAPv4 analysis. **d**, Multi-model mean D26 trends of 10 HighResMIP models from 1972 to 2014 (Supplementary Table 3).

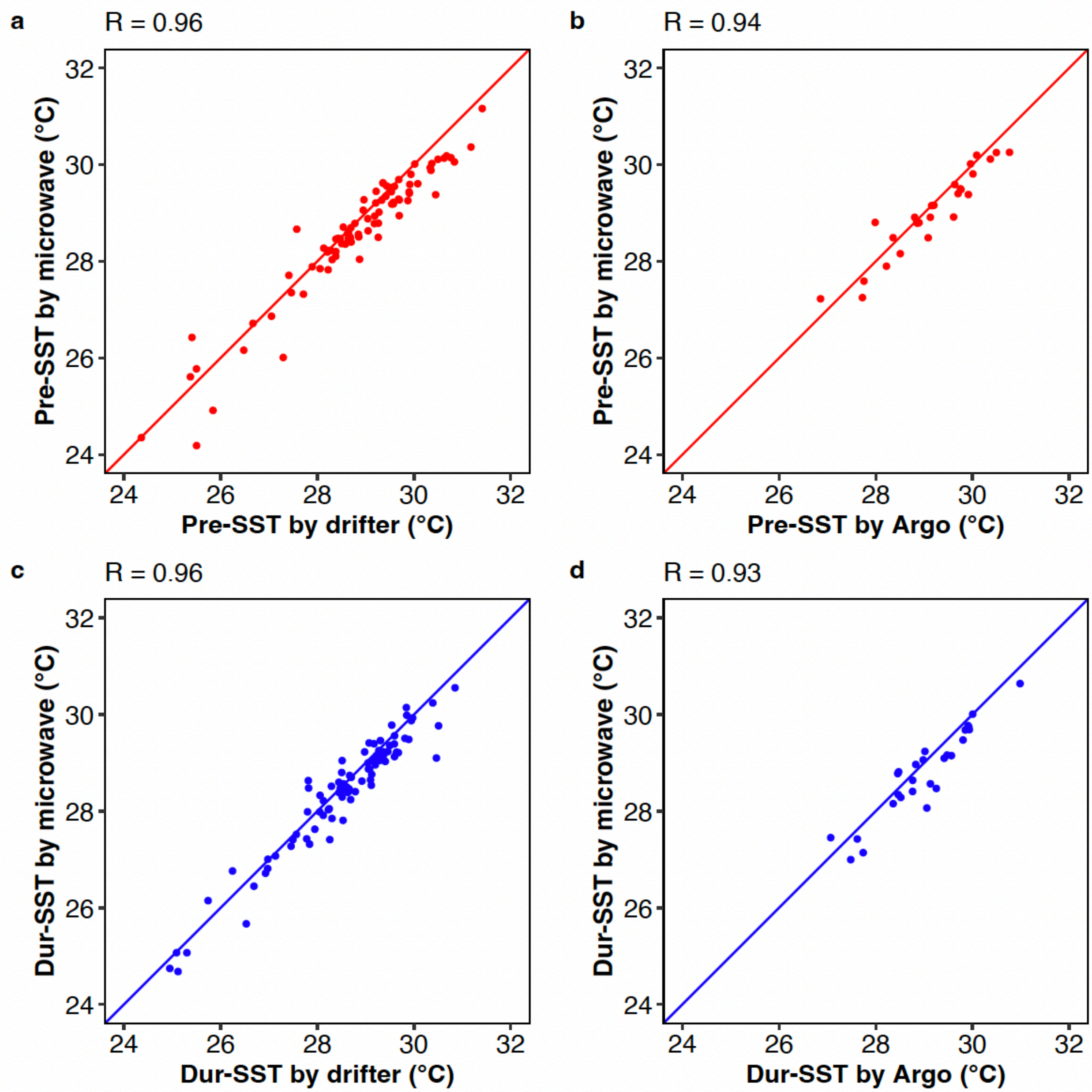

Supplementary Fig. 9 | Comparisons of SSTs from different sources. a, Comparisons of mean SSTs from Days −10 to −4 between microwave satellite data and drifter data. **b**, Same as **a** but between the microwave satellite data and the Argo float data. **c**, Same as **a** but for SSTs on Day 0. **d**, Same as **b** but for SSTs on Day 0. Correlation coefficients are shown in the upper left corners of each panel.

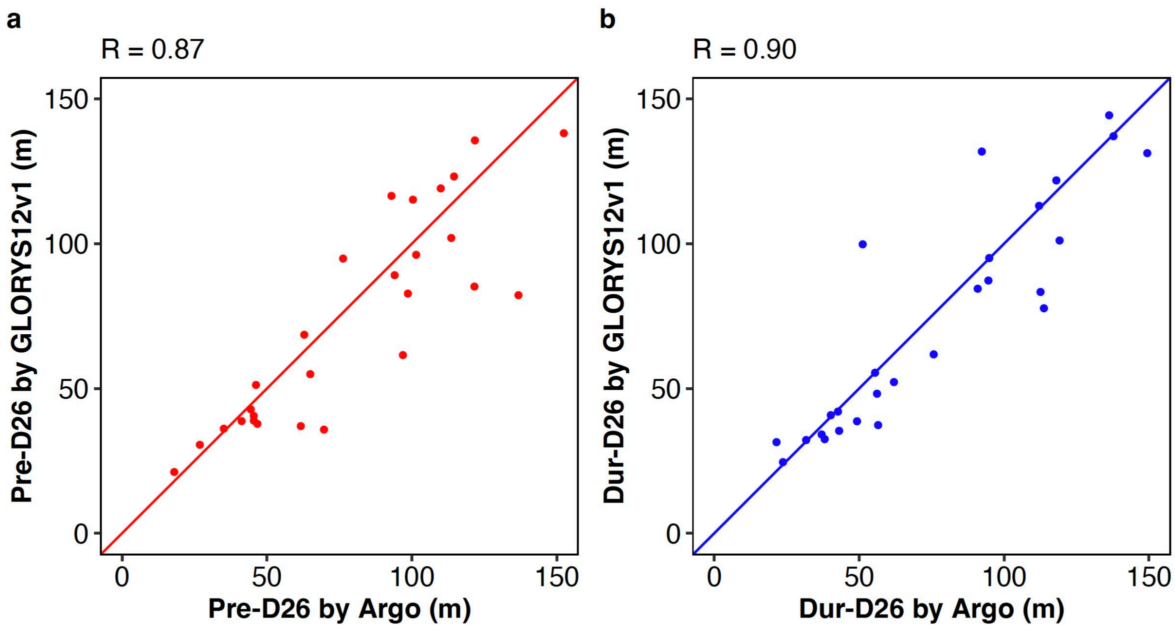

Supplementary Fig. 10 | Comparisons of D26 from different sources. **a**, Comparisons of median D26 from Days −10 to −4 between GLORYS12v1 data and Argo data. **b**, Same as **a** but for D26 on Day 0. Correlation coefficients are shown in the upper left corners of each panel.

Supplementary Table 1 | Empirical formulas for determining the Ekman layer depth and corresponding references.

Empirical formula	Parameter value	Ekman depth at 10°N/S under 10-m wind of 10 m s^{-1}	Reference
$D_{\mathrm{E}} = \dfrac{\alpha W_{10}}{\sin\lvert\phi\rvert}$	$\alpha = 3.66$	211 m	M77 (ref.[1])
$D_{\mathrm{E}} = \dfrac{\beta W_{10}}{\sqrt{\sin\lvert\phi\rvert}}$	$\beta = 4.3$	103 m	PP83 (ref.[2])
$D_{\mathrm{E}} = \dfrac{\gamma\sqrt{C_d \rho_a W_{10}^2/\rho_o}}{2\Omega \sin\lvert\phi\rvert}$	$\gamma = \begin{cases} 0.25\text{–}0.4 \text{ (PS99)} \\ 0.5 \text{ (WH04)} \end{cases}$ $C_d = 1.4 \times 10^{-3}$, $\rho_a = 1.3 \text{ kg m}^{-3}$, $\rho_o = 1025 \text{ kg m}^{-3}$, $\Omega = 7.2921 \times 10^{-5} \text{ s}^{-1}$	132–210 m (PS99) 263 m (WH04)	PS99 (ref.[3]) WH04 (ref.[4])

In the formulas above, W_{10} is the 10-m wind speed and ϕ is the latitude. The maximum and minimum values of the PS99 formula are denoted as PS99$_{max}$ and PS99$_{min}$, respectively. The differences between M77 and PS99$_{max}$ are very small, so PS99$_{max}$ is not shown in Fig. 3. Note that the classical Ekman theory is derived with ideal assumptions including a steady state, no background currents, and linearity. Thus, there is a caveat in applying the steady and linear classical Ekman theory to TCs. The presence of western boundary currents and mesoscale oceanic eddies challenges the assumption of linearity in classical Ekman theory. However, using a time-dependent[5] and nonlinear[6] Ekman theory only leads to quantitative differences, and it does not alter our conclusions.

Supplementary Table 2 | Hierarchy of HighResMIP models analysed in this study.

	HadGEM3-GC31-HM	HadGEM3-GC31-LL	HadGEM3-GC31-MM
Ensemble Member for *hist-1950*	r1i1p1f1 r1i2p1f1 r1i3p1f1	r1i1p1f1 r1i2p1f1 r1i3p1f1 r1i4p1f1 r1i5p1f1 r1i6p1f1 r1i7p1f1 r1i8p1f1	r1i1p1f1 r1i2p1f1 r1i3p1f1
Ensemble Member for *control-1950*	r1i1p1f1	r1i1p1f1	r1i1p1f1
Ensemble Member for *highres-future*	r1i1p1f1 r1i2p1f1 r1i3p1f1	r1i1p1f1 r1i2p1f1 r1i3p1f1 r1i4p1f1	r1i1p1f1 r1i2p1f1 r1i3p1f1
Atmos Nominal Resolution	50 km	250 km	100 km
Ocean Nominal Resolution	25 km	100 km	25 km
Total time span	404 years	765 years	404 years

Supplementary Table 3 | Suite of HighResMIP coupled model outputs for the *hist-1950* experiment analysed in this study.

Model name	Ensemble member	Atmos nominal resolution	Ocean nominal resolution
CNRM-CM6-1	r1i1p1f2	250 km	100 km
EC-Earth3P	r1i1p2f1	100 km	100 km
EC-Earth3P-HR	r1i1p2f1	50 km	25 km
ECMWF-IFS-HR	r1i1p1f1	25 km	25 km
ECMWF-IFS-LR	r1i1p1f1	50 km	100 km
HadGEM3-GC31-HM	r1i1p1f1	50 km	25 km
HadGEM3-GC31-LL	r1i1p1f1	250 km	100 km
HadGEM3-GC31-MM	r1i1p1f1	100 km	25 km
MPI-ESM1-2-HR	r1i1p1f1	100 km	50 km
MPI-ESM1-2-XR	r1i1p1f1	50 km	50 km

Supplementary References

1 Madsen, O. S. A realistic model of the wind-induced Ekman boundary layer. J. Phys. Oceanogr. 7, 248–255 (1977).

2 Pond, S. & Pickard, G. L. Introductory Dynamical Oceanography (Gulf Professional Publishing, 1983).

3 Price, J. F. & Sundermeyer, M. A. Stratified Ekman layers. J. Geophys. Res.: Oceans 104, 20467–20494 (1999).

4 Wang, W. & Huang, R. X. Wind energy input to the Ekman layer. J. Phys. Oceanogr. 34, 1267–1275 (2004).

5 Lewis, D. M. & Belcher, S. E. Time-dependent, coupled, Ekman boundary layer solutions incorporating Stokes drift. Dynam. Atmos. Ocean 37, 313–351 (2004).

6 Pedlosky, J. On the weakly nonlinear Ekman layer: thickness and flux. J. Phys. Oceanogr. 38, 1334–1339 (2008).